Anatomy of Strike Slip Fault Tsunami-genesis

Ahmed Elbanna[a], Mohamed Abdelmeguid[a], Xiao Ma[a], Faisal Amlani[b], Harsha S. Bhat[c], Costas Synolakis[d,e,f], and Ares J. Rosakis[g,1]

[a]Department of Civil and Environmental Engineering, University of Illinois at Urbana Champaign, Urbana, Illinois; [b]Department of Aerospace and Mechanical Engineering, University of Southern California, Los Angeles, USA; [c]Laboratoire de Géologie, École Normale Supérieure, CNRS-UMR 8538, PSL Research University, Paris, France; [d]Department of Civil and Environmental Engineering, University of Southern California, Los Angeles, CA 90089-2531, USA; [e]Research Centre for Atmospheric Physics and Climatology, Academy of Athens, 84 Solonos str., 10680 Athens, Greece; [f]Department of Environmental Engineering, Technical University of Crete, Polytechnioupoli, 73100 Chanea, Greece; [g]Graduate Aerospace Laboratories, California Institute of Technology, Pasadena, CA 91125

This paper is a non-peer reviewed preprint submitted to EarthArXiv.

Tsunami generation from earthquake induced seafloor deformations has long been recognized as a major hazard to coastal areas. Strike—slip faulting has generally been believed as insufficient for triggering large tsunamis, except through the generation of submarine landslides. Herein, we demonstrate that ground motions due to strike–slip earthquakes can contribute to the emergence of large tsunamis (>1m) under rather generic conditions. To this end, we have developed a computational framework that integrates models for earthquake rupture dynamics with models of tsunami generation and propagation. The three-dimensional time-dependent vertical and horizontal ground motions from spontaneous dynamic rupture models are used to drive boundary motions in the tsunami model. Our results suggest that supershear ruptures propagating along strike–slip faults, traversing narrow and shallow bays are prime candidates for tsunami generation. We show that dynamic focusing and the large horizontal displacements, characteristic of strike-slip earthquakes on long faults, are critical drivers for the tsunami hazard. These findings point to intrinsic mechanisms for sizeable tsunami generation by strike–slip faulting, which do not require complex seismic sources, landslides, or complicated bathymetry. Furthermore, our model identifies three distinct phases in the tsunamic motion; an instantaneous dynamic phase, a lagging coseismic and a classical postseismic phase, each of which may affect coastal areas differently. We conclude that near-source tsunami hazards and risk from strike-slip faulting need to be re–evaluated.

Tsunamigenesis in bays | Strike–slip Faults | Super–shear ruptures | Vertical and horizontal bathymetry motions

Tsunamis are classically defined as long free–surface water waves generated by impulsive geological events (1). Tsunamis may be triggered by earthquakes, volcanoes, landslides or slumps, submarine gas releases and meteorite impacts. Over the past century, tsunamis alone have been responsible for the loss of hundreds of thousands of lives and trillions of dollars in damage to the environment and built infrastructure (2, 3). This makes tsunamis among the most destructive natural hazards. Quantitative and predictive modeling of tsunamis is crucial for reducing the impact of these events and for enabling better preparedness plans.

Generally the size of the vertical seafloor motion is associated with the tsunami size. Massive tsunamis are generally attributed to great earthquakes along subduction–zone plate boundaries, such as the 2004 M$\sim$ 9.2 Sumatran and the 2011 M$\sim$ 9.0 Tohoku–Oki events. McKenzie and Jackson (2012) further suggested that the release of gravitational energy due to movement of large land masses during these earthquakes may further amplify the resulting tsunami (4). Strike–slip faults which generally generate small seafloor vertical displacements are generally considered unfavorable for tsunami generation (5) . Field observations, however, suggest that in many cases (6–10) strike–slip motion can indeed generate tsunami waves, supposedly, by triggering landslides (11). Even though a small fraction of all tsunamis studied this far are believed to be triggered by strike-slip motion (12), the devastating humanitarian impact warrants further investigation into this particular mechanism for tsunamigenesis.

The September 2018 Mw 7.5 Sulawesi earthquake occurred on the Palu–Koro (P–K) strike–slip fault system and caused an unexpected localized tsunami that was atypical in its magnitude, for this type of fault motion(13). Bao et al. (2019) and Socquet et al. (2019) were among the first to recognize the supershear nature of this earthquake (14, 15). Several authors (14, 16–18) have postulated that submarine landslides, triggered by the earthquake's strong ground motion, were the primary source for the devastating tsunami. Ulrich et al. 2020 (19) argued that the earthquake displacements were critical to the tsunami generation. Using a 3D dynamic rupture model that emulated the earthquake propagation on the geometrically complex P–K fault system, and coupling it with the 2D shallow water-wave equations, they demonstrated that the fault slip, which included a non–negligible rake and dip slip components, may only trigger tsunami waves of the order of a meter. However, their shallow water formulation did not account explicitly for dynamic bathymetry. Moreover, their conclusions are confounded by the specifics of the complex Palu bay bathymetry and the complex geometry of the fault system.

Amlani et al. (20) utilized near-fault GPS data to first conclusively demonstrate that the P–K rupture was indeed supershear. They then recovered a crucial term in the shallow water wave equation by including time–dependent seafloor motions, and thus insured correct mass conservation (21). This forcing was implemented in the context of a 1D nonlinear shallow water wave model (NLSE) and a simple bathymetry that was driven dynamically by the vertical components of the motion computed from a 3D dynamic rupture simulation of a supershear earthquake along a strike–slip fault. They showed that explicitly accounting for the dynamic source effects uncovers high frequency details in the early phases of the tsunami motion, which may get missed, if only the static seafloor displacements are used. However, they did not consider the effect of horizontal displacements in the ground motion on deforming the bathymetry. Furthermore, their 1D model could not account for the dramatic focusing effect introduced by water waves diffracting at the apex of any narrow bay. These limitations possibly led to a noticeable underprediction of the calculated amplitude of the waves.

The question still remains whether generic strike-slip faults can generate large tsunamis in the absence of secondary sources, such as coseismic underwater landslides. This question has important ramifications, as several metropolitan areas worldwide are located near bays (7, 8, 22–24) that are traversed by strike-slip faults similar to the P–K system. Furthermore, while early warning for farfield tsunamis (1, 25, 26) based on hydrodynamic inversions is now fairly routine, at least in the North Pacific, little or no early warning is possible for nearfield tsunamis in which the tsunami originates just a few kilometers away from the coastline. Most field scientists agree that this far, for coastal residents, earthquake shaking is the warning for an impeding tsunami from a nearshore source.

To shed light on the basic mechanisms through which strike–slip faults may cause damaging tsunamis, we have developed a computational framework that integrates mechanistic models for earthquake rupture dynamics with hydrodynamic models for tsunami generation and propagation. Possibly with few exceptions, in tsunami models, the initial condition is computed according to the static algorithms of Mansinha and Smylie (27), subsequently parametrised by Okada (28), which translates finite fault models into static seafloor displacements. In recent years there has been an increased interest in developing models that account for dynamic generation (19, 29–31). Here, we focus on a planar strike-slip fault traversing a shallow bay with a simple geometry. Tsunami evolution over a more complex bathymetry may hide the effects of the dynamic rupture, or, in other words, we need to understand the basic phenomenology first, before applying our model to complex geophysical geometries. Our approach is thus designed to unravel the underlying physics governing tsunami generation due to strike–slip faulting.

The 2018 Palu earthquake and tsunami highlighted the complex dynamics of tsunamis generated by intersonic earthquakes. In supershear, or intersonic earthquakes (32–38), the rupture tip propagates faster than the shear wave speed(39–41). This leads to emergence of large localized deformation bands along the shear shock wave fronts, also known as Mach cones (32, 33, 36, 37, 42). Dunham and Bhat (2008) proved the presence of a second Mach front associated with Rayleigh waves that carry significant vertical motion, moderately attenuated, to large distances (36). When such earthquakes occur within a narrow bay, the associated large horizontal displacements, as well as the moderately–attenuated vertical displacements (32, 37, 43), along the shear and Rayleigh shock wave fronts will cause significant motion in the bay boundaries, which just as with a paddle wavemaker, could lead to the displacement of large volumes of water. Furthermore, in these scenarios, the triggered tsunami may exhibit multiple characteristic time scales ranging from a few seconds to several minutes.

In the following sections, we investigate what turned out as synergistic interactions between rupture speed, seafloor ground motions, and bay geometry. We also examine several distinct features of the tsunami, including the emergence of an instantaneous dynamic phase, and a slower co–seismic phase, both of which lead to a classical gravity–driven post-seismic phase.

Coupled earthquake–tsunami framework

Earthquake Model. We model a bilaterally expanding earthquake rupture by solving the elastodynamic wave equation, for the bulk displacement field $u_j(x_j, t)$ for $j = 1, 2, 3$, in a 3D linear elastic medium surrounding a rectangular planar fault. We prescribe absorbing boundary conditions along the lateral and bottom boundaries of the domain to minimize artificial wave reflection due to simulation domain truncation. The top boundary, which corresponds to the seafloor, is modelled as a free surface. We impose an initially uniform shear stress everywhere on the fault surface except for a small circular localized region which we overstress to forcefully nucleate the rupture. The initial shear stress is applied along the fault strike direction to constrain the fault slip to be horizontal. Furthermore, a uniform compressive stress acts on the fault.

The fault strength is governed by a linear slip-weakening frictional law. Fault slip starts at a point when the shear stress reaches the static shear strength level, given by the product of the static friction coefficient and the compressive normal stress. The stress then decreases linearly, with increasing slip over a characteristic slip–weakening distance, to a constant value; the dynamic shear strength, set by the product of the uniform dynamic friction coefficient and the compressive stress. The terminal speed of the nucleated rupture depends on the fault stress level as measured by the strength parameter S, which is given by the ratio of two stress measures(40). The first is the difference between static shear strength and initial shear stress. The second is the difference between initial shear stress and the dynamic shear strength. The S parameter thus quantifies the proximity of the fault initial stress state to its static strength. High S values, corresponding to low-stressed faults, generally favor sub-Rayleigh ruptures with the rupture propagation speed limited by the Rayleigh wave speed. Low values of S, corresponding to high-stressed faults, enable the rupture tip to break the shear wave speed barrier and become supershear, propagating at intersonic speeds. In this work, we vary the value of the initial shear stress to simulate both supershear and sub-Rayleigh ruptures. Details of the earthquake model is given in the Materials and Methods section.

Tsunami Model. We model the tsunami initiation and subsequent propagation in the bay using the 2D nonlinear shallow water equations (NWSE) assuming an inviscid, and incompressible flow model (29, 44). The coupling between the earthquake and tsunami models is realized through the time–dependent 3-D seafloor displacement and velocity fields computed from the dynamic rupture simulation, and then imported to the tsunami model as time–dependant boundary motions. Specifically, we solve the following set of nonlinear equations (45):

[1] To whom correspondence should be addressed. E-mail: elbanna2@illinois.edu

$$h^*_{,t} + (\hat{u}h^*)_{,1} + (\hat{v}h^*)_{,2} = 0 \quad [1a]$$

$$\hat{u}_{,t} + \hat{u}\hat{u}_{,2} + \hat{v}\hat{u}_{,2} + gh^*_{,1} = gH_{,1} \quad [1b]$$

$$\hat{v}_{,t} + \hat{u}\hat{v}_{,1} + \hat{v}\hat{v}_{,2} + gh^*_{,2} = gH_{,2} \quad [1c]$$

Here, x_1 and x_2 are the horizontal spatial coordinates, while x_3 is the vertical spatial coordinate. t is time, $H = H(x_i, t)$ is the depth of the bay for $i = 1, 2$, $\hat{u} = \hat{u}(x_i, t)$, $\hat{v} = \hat{v}(x_i, t)$ for $i = 1, 2$ are the depth–averaged horizontal water velocities, $(.)_{,i}$ denotes the differentiation of the relevant variable with respect to coordinate x_i, and g is the gravitational acceleration. We define $h^* = h + H$, where h is the vertical sea surface displacement measured from the initially undisturbed sea surface level $x_3 = 0$. We note that in Eq.1a, $h^*_{,t} = h_{,t} + H_{,t}$. Thus, by accounting explicitly for the $H_{,t}$ term, we are utilizing both the time–dependant seafloor displacements and seafloor velocities in the dynamic model and not just the time–dependent displacements.

For a general bathymetry, horizontal motions could contribute to the free–surface motion, as recognized by Tanioka and Satake (46). For a seafloor displacement $u_i(x_i, t)$ and initial static bathymetry profile $H_o(x_i) = H(x_i, 0)$, the sea floor motion is computed by taking into account horizontal and vertical displacements(47):

$$H(x_i, t) = H_o(x_i - u_i(x_i, t)) - u_3(x_i, t), \quad i = 1, 2 \quad [2]$$

The expression in Eq.2 is general enough to account for any slope and is not restricted by the smoothness of the bathymetey or the amount of deformation. We therefore prefer it, compared to other more widely used approaches that involve incorporation of the horizontal motions approximately through computing the first order Taylor expansion of the Eq.2 (19, 48, 49). Details of the tsunami model are given in the Materials and Methods section.

Results

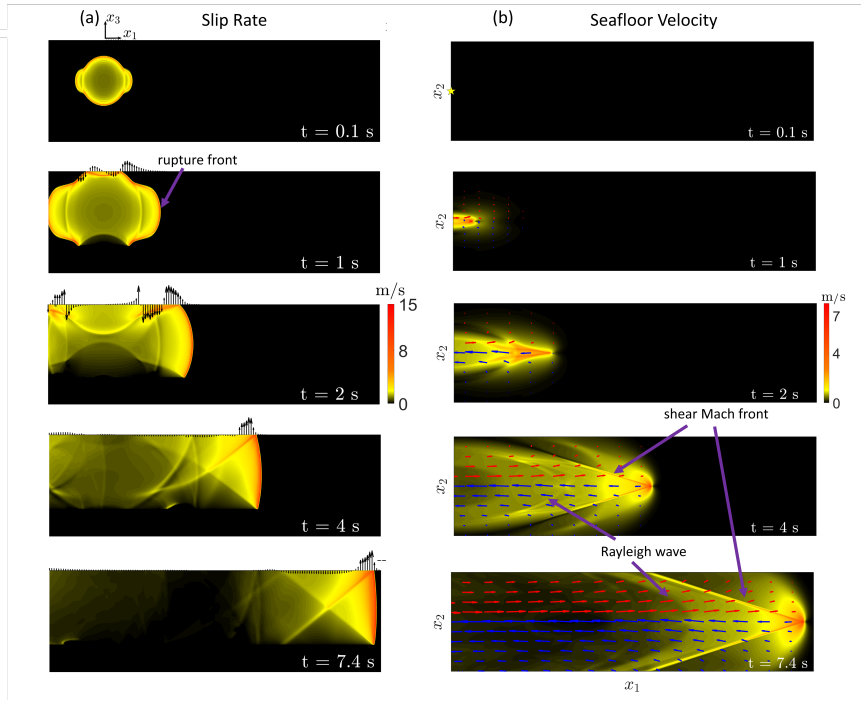

Fig. 1. Evolution of a supershear rupture on a right lateral strike slip fault.. Snapshots of the (a) fault slip rate, and (b) seafloor velocity are shown at time 0.1, 1, 2, 4, and 7.4 s. The rupture, nucleated at depth in within an overstressed region, subsequently expanded to reach the surface and propagated at super-shear speeds after saturating the seismogenic zone. On the seafloor, shear shock wave fronts (Mach cones) emerge and sharpens, extending away from the fault with little attenuation, as the rupture continues to propagate. Vectors of the in-plane displacements are superimposed on seafloor velocity contours to demonstrate the direction of the motion on seafloor (scale shown in figure). Rupture features such as the shear mach cone and trailing Rayleigh wave are highlighted.

Fig.4 shows the development of the supershear rupture on a right lateral strike–slip fault in terms of fault slip rates and sea floor particle velocities. The earthquake nucleates at the hypocenter, and propagates, first at sub–Rayleigh speeds, toward the free-surface as it saturates the seismogenic zone, before transitioning into the supershear mode. Fig.4a demonstrate snapshots of the slip rate on the fault surface at different times. Initially (t = 0.1 s) we observe the nucleation of the earthquake within the overstressed region. Then we observe the subsequent rupture expansion and the clear delineation of the rupture fronts which continue to propagate towards the apex saturating the seismogenic zone (t = 1.0 s). As the rupture front reaches the top

and bottom boundaries of the domain, waves are reflected back. At this stage, shock fronts start to develop on the fault surface, accompanying the transition to supershear propagation (t=2.0 s) as we will discuss shortly in Fig.4b . The shock fronts are capped by the locked-slipping interface at the bottom edge of the fault surface, resulting in another set of reflected waves (t= 4.0s). The figure also shows vectors of seafloor vertical velocities superimposed on the slip rate snapshots to highlight a few observations: (i) the sea floor vertical velocity is highest in the vicinity of the rupture tip as well as the trailing sub-Rayleigh wave front (all subplots); (ii) supershear transition and the onset of the shock wave fronts are accompanied by pronounced vertical sea floor velocities (t= 2.0s), (iii) as the rupture continues to propagate, the vertical velocities continue to be high within the shock wave front region. Velocities elsewhere are diminished in comparison (t=4.0s & 7.4 s); and (iv) the vertical velocities are not monotonic. They alternate between positive and negative values along the fault strike The pronounced vertical velocity field that persists around the rupture tip and within the shock wave region as the dynamic rupture propagates has a direct imprint on the generated tsunami as will be discussed shortly.

Fig.4b illustrate the magnitude of the particle velocity on the seafloor, focusing on the forward-propagating rupture tip,at different times. Initially, there is no visible disturbance as the waves, emanating from the rupture at depth, have not reached the surface yet (t = 0.1 s). Then, as the rupture grows, parts of the rupture front reaches the surface and we observe the onset of intense ground motion (t = 1.0 s). As the rupture expands, we observe key characteristics of the supershear propagation including (i) the sharp increase in the sea floor particle velocity during the rapid acceleration of the rupture from sub-Rayleigh to supershear speeds (t = 2 s), (ii) the development of shear shock wave fronts, emerging due to the coherent interference of shear waves trailing the propagating rupture tip, which gradually extends into the bulk away from the fault (t= 4.0 s).(iii) the development of a secondary Rayleigh wave (34, 37, 42) front that trails the shear shock wave front, and which emerged due to the rapid acceleration of the rupture during supershear transition (t= 4.0 s), and (iv) the sharpening of the shock fronts and their expansion into further distances within the bay without significant attenuation. (t=7.4 s).

At all times, the rupture tip always lags behind the pressure wave front. The arrows in Fig.4b represent the magnitude and direction of the resultant inplane displacement. Since the fault slip has a right lateral sense, the seafloor is pushed away from the fault on the top side of the forward–propagating rupture tip (negative side) while it is pulled towards the fault surface on the bottom side (positive side) (t = 1 s). As the rupture further expands, the magnitude of the in–plane displacements, reflected by the size of the arrows, increase but the sense of motion just described above persists (t=2, 4, and 7.4 s). These in–plane displacements are critical for the tsunami dynamics as they may induce large seafloor variations. In particular, if such a fault is traversing a bay, we expect that on the "negative" side of the fault, the slopes of the bay are pushed away, which is equivalent to a downward movement of the seafloor. On the "positive" side of the fault, the slopes are pulled towards the fault surface, and this is equivalent to an upward movement of the seafloor. The equivalent vertical motion of the seafloor due to the bulk in–plane displacements are to be added to the direct vertical motion coming from the vertical displacements due to the strike slip motion. The synergetic interaction between the displacement components enrich the tsunami dynamics, on different time scales, as we will discuss shortly.

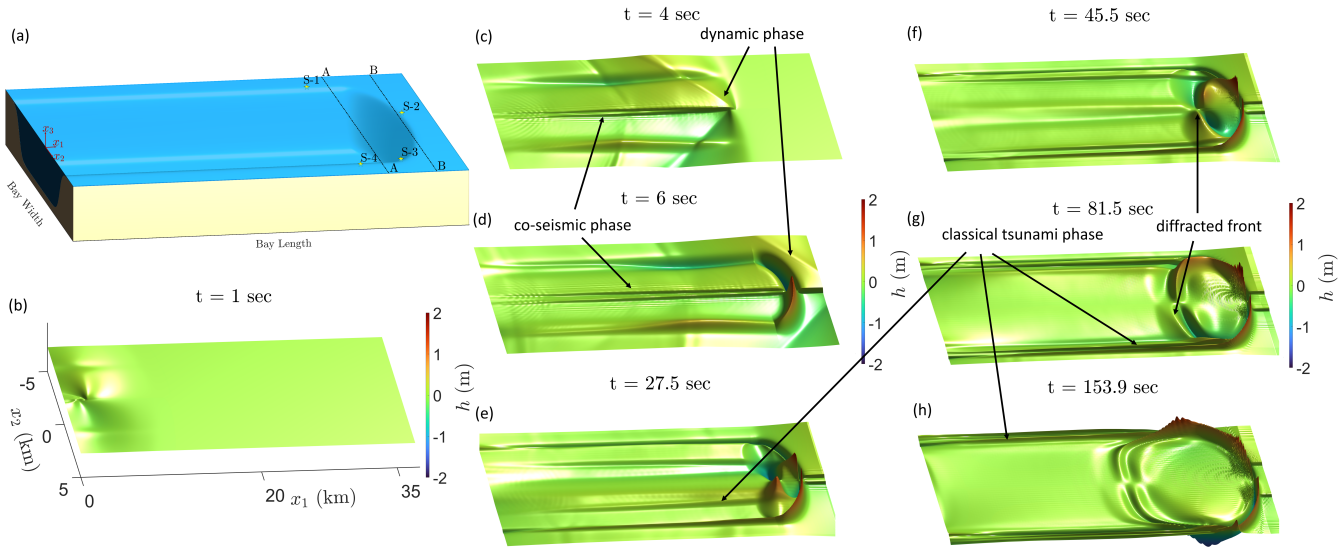

Fig. 2. Evolution of the earthquake induced tsunami in a basin traversed by a super-shear rupture. (a) Basin bathymetry, with various measuring stations and sections marked. (b-h) Snapshots of the super-shear tsunami scenario at 1, 4, 6, 27.5, 45.5, 81.5 and 153.9 s, shown sequentially from left to right. Colors indicate the sea surface height (h) relative to the undisturbed water level. Panels (b,c,d) correspond to the "dynamic tsunami generation phase", and the rest to the "post-seismic classical tsunami generation phase". The evolution of different tsunami generation mechanisms, as well as, coseismic rupture signatures are observed.Note the common color scale bar between all the subplots. An alternative representation for these surface plots, in which multiple scale bars, adjusted for the local water surface peak amplitude in each displayed time step, is provided in SI Appendix, Fig. S2-3

We now turn our attention to the tsunami dynamics. Fig.2a illustrates the bathymetry of the simulated bay. We record the water surface amplitude at a number of stations located at various locations within the bay and along the coastline. We note

that a spectrum of time scales emerge for near-source tsunamis, like the one modeled here, that is usually overlooked in the more commonly studied far-source tsunamis. Specifically, we define:

1. An instantaneous dynamic tsunami phase (on the scale of few seconds as shown in Fig.2b-d) in which the water surface is directly and almost instantaneously driven by the coseismic motion of the sea floor ($H_{,t} \neq 0$), even at large distances from the fault line, because of the unattenuated action of the shock waves.

2. A coseismic tsunami phase that is initiated by the dynamic seafloor motion, but propagate much slower than the dynamic one, due to the diminishing effect of ($H_{,t}$) term as the rupture front zips along the fault plane (as shown in Fig.2b-d).

3. A much slower, classical, post-seismic tsunami (on the scale of tens of seconds to several minutes as shown in Fig.2e-h), driven by gravity and is prone to diffraction and amplification by the bay geometry.

While this classical postseismic tsunami is set in motion by the history of both the dynamic and coseismic tsunami phases, its propagation has no input from the time dependent motion of the bathymetry ($H_{,t} = 0$). In the case of farfield tsunamis, the postseismic tsunami occurs on the scale of tens of minutes to hours. Therefore neglecting the initial dynamic phase which occurs on the time scale of seconds may be justified.

Fig.2b-d show the dynamic, and coseismic, tsunami generation phases commensurate with the earthquake nucleation and subsequent propagation. Since the rupture speed is nearly two orders of magnitude larger than the speed of gravity sea-surface long waves, there is a negligible effect of shallow water dispersion, and the tsunami dynamics is entirely dominated by the rapid variation in the seafloor topography. This is why, we almost immediately observe features in the free surface profile that are identical to the features reported for the seafloor deformation from the earthquake simulation, including the shock wave fronts and the trailing Rayleigh wave pulse. These features also reflect the strong signature of the sea floor vertical velocity highlighted in Fig.4b

Furthermore, Fig.2c-d shows that the horizontal motion of the bathymetry due to the ground motion profile shown in Fig.4b during the dynamic rupture, results in a pronounced uplift in the water surface at the banks of the bay. These are recognized by the ridge-like features that very quickly form local water disturbances that emerge on both sides of the bay. Moreover, as the strike slip rupture further propagates, we observe the emergence of secondary water wave fronts that join at the rupture tip and form a very shallow angle with the fault parallel direction. These fronts belong to the co-seismic tsunami phase which subsequently propagate away from the fault at speeds proportional to $\sqrt{gH}$ as part of the classical, gravity driven, post-seismic tsunami once the magnitude of the ($H_{,t}$) term becomes negligible as the dynamic rupture exits the simulation domain.

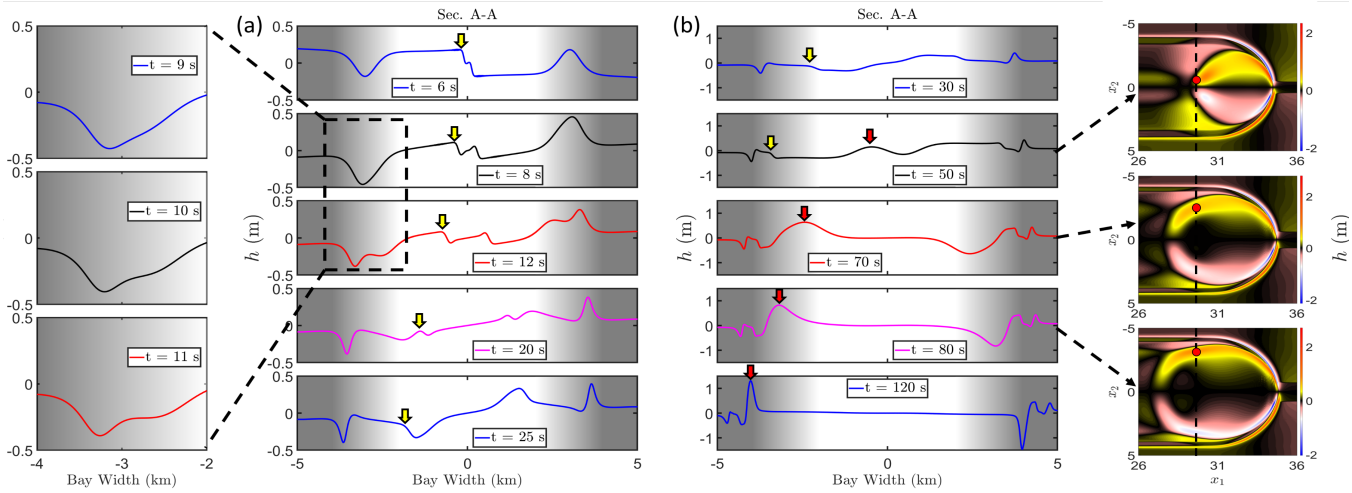

Fig. 3. Snapshots of sea surface height h for cross section A-A. The snapshots correspond to different phases of tsunami generation associated with different time scales. (a) Late dynamic tsunami phase to early post-seismic phases including co-seismic tsunami phases at times 6, 8, 12, 20 and 25 s. (b) Fully developed post-seismic tsunami phase at times 30, 50, 70, 80 and 120 s. Grey scale indicate the bathymetry variation along the cross section where the depth varies from 700 m to 10 m over a distance of 2 km. The evolution of tsunami waves over the banks of the bay is emphasized in left zoom in. Contour plots (right) show the diffracted tsunami waves, which are part of the classical tsunami phase, propagating toward cross section A-A. A More detailed breakdown for the dynamic tsunami phase between times t = 4.0 s and t = 7.5 is provided in SI Appendix, Fig. S4.

Fig.2e-h further demonstrate the post-seismic tsunami onset and propagation as well as its interaction with the apex region. The tsunami wave, mentioned above, develops emanating from the fault surface and propagates outward towards the coastlines in either direction. These waves have an initial amplitude set by the vertical displacement at the seafloor due to the earthquake. While strike slip faults generate pre- dominantly horizontal displacements, there still is a non-negligible vertical component that emerges at the seafloor to satisfy the plane stress condition at the free surface. This is true especially when these ruptures are supershear in which case, this out of plane displacement is not localized at the rupture tip but extends along the Mach fronts(43, 50). Simultaneously, gravity driven tsunami waves start to evolve over the banks of the bay. These waves are created

following the initial dynamic disturbance that resulted from the coupling between the horizontal motion of the bathymetry and the uplift/depression of the sea surface. We observe that this initial disturbance is dispersed into two waves, one travels toward the interior of the bay and the other travels towards the coast. The coast-heading waves are a direct threat for the coastal community. In the apex region, the water wave amplitude reaches 2.6 m and persistently propagates through the shallow portion of the coastline without much attenuation. We note that these waves form on time scales of tens of seconds and it takes them only a couple of minutes to cover hundreds of meters beyond the shoreline into what is supposed to be the habitable coast. This highlights the unique hazard poised by this type of tsunamis as they leave very little time for early warning.

Another remarkable phenomenon relates to the diffraction of the tsunami waves as they interact with the apex region. We observe that the high amplitude initial disturbance, set by the dynamic displacements of the slopes at the apex, travel radially backward toward the interior of the bay hitting coastal regions located further back. The amplitude of these diffracted waves continue to grow as they propagate backwards due to the amplification by the shoreline bathymetry and interaction with other waves existing in the bay. The complex water wave pattern that emerge from the simple bay geometry and simple earthquake source characteristics, highlights the importance of considering the strike slip horizontal motions when modeling tsunami hazard in narrow bays as the interaction of the rupture dynamics with the slopes may contribute to substantial water uplift, even in the absence of triggered landslides.

To gain further insights into the characteristics of these different tsunami generation mechanisms, we investigate the spatio-temporal evolution of the water level. Fig.3a and b show snapshots of the water level along Sec. A–A shown in Fig.2a, during the dynamic, co-seismic, and the post-seismic tsunami generation phases respectively. Several observations follow. Even early on (t = 6.0 s), we observe the onset of the classical tsunami as manifested by the discontinuity in the water surface profile, highlighted by the yellow arrow, close to the fault location. The coupling between the horizontal motion of the slopes and the vertical displacement of the sea surface leads to the emergence of a pronounced crest and a valley in the water surface profile over the right (positive side)and left (negative side)banks respectively. Subsequently, each of these initial disturbances results in two propagating fronts, one expanding in the direction of the coast and the other in the direction of the bay, as detailed in the inserts in Fig.2 over the time period t = 8.0 s to 12.0 s. The speed of the fronts is governed by the varying water depth.The front propagating towards the bay travel faster. At $t = 25$ the front propagating toward the bay coalesces with the classical tsunami wave propagating away from the fault surface, to form a larger amplitude wave.

Fig.3b, whose vertical scale has been adjusted by a factor of three compared to Fig3b, highlights the post seismic tsunami generation phase. The classical tsunami wave (marked by the yellow arrow) propagates further toward the coast, whilst the radially traveling wave front from the apex (marked by the red arrow and shown in the contour plots to the right) expand further toward the coast. Sudden increase in the water level is observed as the radially traveling wave front approach the coastline due to amplification by the diminishing water depth. We observe that these high amplitude waves emerge at different focal points, long past the initial disturbance of water level and constitute a substantial hazard for the coastal environment. It is important to note that the solution is not anti-symmetric about the fault surface. This deviation is most obvious at $t = 120$ seconds, where the magnitude of the water level is higher on the right side of the bay ($h = -1.6$ m) compared to the left side ($h = 1.3$ m). The lack of perfect antisymmetry is explained by the symmetric nature of the fault normal horizontal displacement u_2, whilst the other two components of seafloor displacement u_1, u_3 are antisymmetric.

In Fig.4 we show snapshots of the in-plane water velocity as vectors superposed on the water surface height during the different tsunami generation phases. Fig.4a shows that the arrival of the rupture tip to the apex at time $t = 6$ s leads to an abrupt variation in the water surface level magnitude. Since the fault slip is right lateral, the flat portions of the sea floor would move up on the negative side of the fault but down on the positive side. This causes the water particle velocity to be pointing downwards (from higher to lower water surface elevations) along the segments of the fault not traversing the coastline slopes. In the meantime, within the apex region, this right lateral motion pushes the shoreline away on the negative side of the fault surface but pulls it back on the positive side. As a result, the water surface is depressed on the negative side while it goes up in the positive side. This causes the water particle velocity in the apex region to point upward along x_2 which is a different direction from the rest of the water surface along the $x_2 = 0$ edge as highlighted by Fig.4a zoom in. Fig.4b shows snapshots of the in-plane water particle velocity at a later time $t = 45.5$ seconds which is well within the post-seismic tsunami phase. Several observations follow in this case: (1) The particle velocity within the deeper portion of the apex region point predominantly in the fault normal direction from the positive side of the fault to the negative side. This sense of motion is the result of the motion of the banks of the bay due to the horizontal displacements of the strike slip fault. Specifically, the slopes on the positive side are pulled towards the fault while those on the negative side are pushed away from it. This leads to the water body having a fault normal momentum component pointing from the positive to the negative sides of the fault. (2) The backward propagating fronts that are diffracted from the apex locally modify the direction of the in-plane particle velocity (Fig.4b zoom in **A**). In particular, we observe that the particle velocity field has a circulatory component in this region. In the region ahead of the diffracted wave, the velocity vectors move along an arc with a clockwise sense of rotation consistent with the geometry of the front. However, behind the diffracted wave, the velocity vectors move along an arc with an anti-clock wise sense of rotation. This sense of motion is opposite to the curvature of the diffracted front and may be explained by the water surface profile in this domain.

Specifically, the anti-clockwise sense of motion seems consistent with the particle velocity pointing from region of higher to lower water surface elevations behind the diffraction front. In the region where the water surface is unperturbed ($h = 0$), the particle velocity maintain its fault normal direction as discussed above. (3) In the shallower parts of the apex region, we observe that the forward propagating wave (up the slope) is compressed while the backward propagating wave (down the

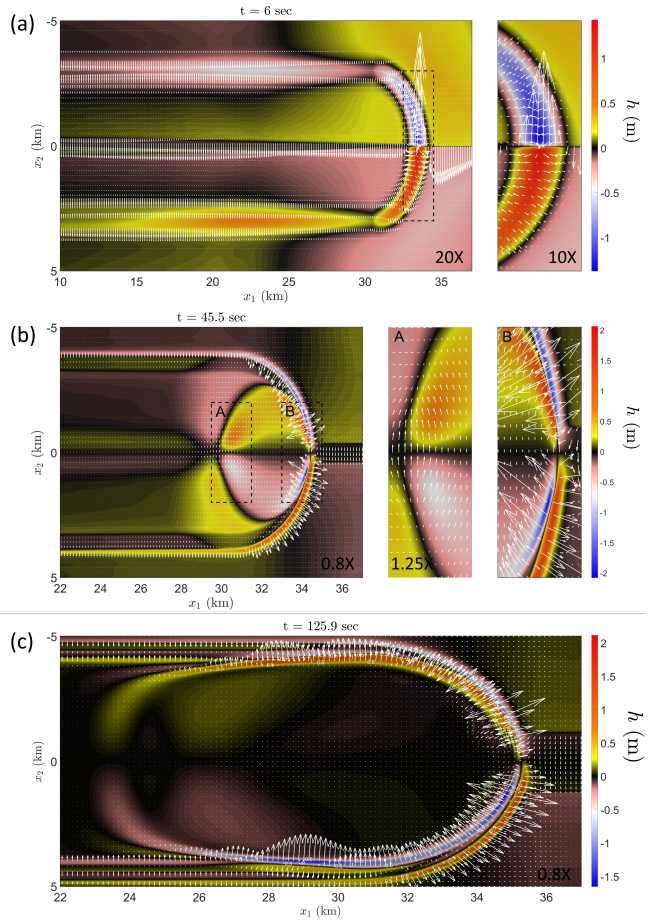

Fig. 4. Snapshots of the in-plane water velocity vectors at different phases of tsunami generation. Colors indicate the sea surface height h relative to the undisturbed water. (a) The "dynamic tsunami generation phase" at 6s. The vector magnitudes are scaled by a factor of 20 for representation. (b) The "postseismic tsunami phase" at 45.5 s, revealing the evolution of the tsunami diffraction pattern and highlighting the structure of water motion near the apex of the bay. The vector magnitudes are scaled by a factor of 0.8 for representation. (c) The "post-seismic tsunami phase" at 125.9 s, revealing the coalescing wave fronts and highlighting the lack of perfect antisymmetry between two sides of the bay. The vector magnitudes are scaled by a factor of 0.8 for representation.

slope) is rarefied. This is accompanied with an increase in the water in-plane particle velocity in both forward and backward directions at the edge of the basin (Fig.4b zoom in **B**). The water in-plane particle velocities are of the order of 1 m/s which may be significant enough to impact the morphology of the shoreline(51). At a later time in Fig.4c, we observe the development of strong difference in the water particle velocity at the lateral sides of the bay. Specifically, the particle velocity over the bay banks on the positive side of the fault is 1.375 times larger the particle velocity on the negative side. This may be explained as follows. On the "positive" side of the fault, the water particle velocity is amplified due to the constructive interference of the diffracted water wave from the apex and the wave generated from the inward motion of the side of the bay which cause an uplift in the water surface. On the "negative" side of the fault, the water particle velocity is reduced due to the destructive interference between the diffracted wave from the apex and the wave generated from the outward motion of the side of the bay which cause a depression in the water surface. This variation in interaction patterns between the different waves propagating within the basin intensifies the contrast in the particle velocity amplitudes at the two sides of the bay.

We also examined tsunami generation in a bay traversed by a sub–Rayleigh rupture. The simulation domains for the tsunami and earthquake models remained the same with identical material properties and dimensions in both the sub-Rayleigh and supershear cases. To generate a sub–Rayleigh rupture, we reduce the value of the initial shear stress, as outlined in the Materials and Methods section.

Fig.5 illustrates the time history of the water surface amplitude for both rupture profiles at the different stations shown in Fig.2a. For the supershear rupture, at station S-1 located at $(x_1, x_2) = (27.5, -4)$ km shown in Fig.5a, the passage of the shock wave front causes an abrupt uplift of water surface of amplitude 0.26 m at time $t = 5.1$ sec. Following this uplift, the water level is depressed corresponding to the arrival of the tsunami wave front that ensued from the horizontal displacement of the slope (up to t 50 s). This is followed by another classical tsunami wave that leads to water resurgence (t 1 min). Finally, the high amplitude wave from the radially propagating front arrives at around 2.25 minutes.Due to the absence of shock waves in the sub-Rayleigh case, we observe a much smaller dynamic tsunami pulse of the order of 0.09m at time $t = 10$s. This is further highlighted in the insert in Fig.5a .The different classical tsunami features are similar across the supershear and sub-Rayleigh

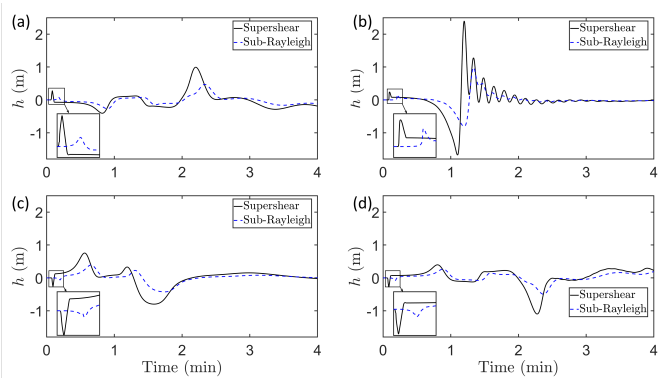

Fig. 5. Comparison between water level histories corresponding to a super-shear and a sub-Rayleigh rupture traversing the same bay. Time histories obtained for the tsunami at stations (a) S-1, (b) S-2, (c) S-3, and (d) S-4. Blue dashed lines correspond to water surface height associated with the sub-Rayleigh rupture at the same locations. The arrival of dynamic rupture induced water wave is highlighted in the zoomed portion.

cases except that the amplitudes in the sub-Rayleigh case are smaller and vary more gradually.

Fig.5b illustrates the water surface dynamics at station S-2 located near the apex of the bay at $(34.5, -1)$ km. Again, we observe an increase in the water level of the order of 0.243m at time $t = 6$ sec, corresponding to the dynamic excitation by the passage of the shock waves. This is followed by a large amplitude depression of the order of (-1.75m) at a time 1.1 min. Subsequently a rapid increase in the water surface is observed with the maximum water level height reaching 2.25m at a time 1.25min. The rapid variation in the water level amplitude (4m) from depression to resurgence, occurring over a time span of just 0.15 min, leads to the emergence of multiple oscillations trailing the peak wave analogous to the impulsive response of an under-damped oscillator. On the other hand, the sub-Rayleigh case shows a smaller range of variation in the water level amplitude as well as smaller extreme values; as low as half the corresponding amplitude in the supershear case. The transition between depression and resurgence is more gradual in the sub-Rayleigh case and as a result the post-peak trailing oscillations are also less visible suggesting a weaker dynamic effect.

At the other side of the bay Fig.5c shows the time history for station S-3 at $(31.5, 3.65)$ km. The dynamic disturbance from the passage of the dynamic rupture is observed at 5.7 seconds and is manifested in the local water surface depression of amplitude 0.257 m. After half a minute we observe the tsunami wave associated with the slope motion, followed by the classical tsunami wave and finally the radially propagating front arrival. All the key features are observed at an earlier arrival time than station S-1, due to the proximity of station S-3 to the apex. Finally, Fig.5d present the time history of water level at station S-4 which is located mirroring station S-1. Accordingly, the time history is similar but with opposite polarity, consistent with the sense of motion on the fault and subsequent displacement of the slopes.

The smaller amplitude of tsunami waves in the sub-Rayleigh case is attributed mainly to the smaller vertical and fault parallel seafloor displacement u_3, u_1 respectively which result in a less pronounced diffraction pattern originating at the bay apex. The effect of smaller vertical displacements is evident in the absence of a strong dynamic tsunami pulse. The weaker fault parallel seafloor displacement leads to diminished bathymetric motions at the apex, resulting in substantially lower uplifts and reduced water wave amplitudes.

These observations have two major implications. First, for a given fault area, a tsunami generated by a supershear earthquake will be larger than that generated by a sub-Rayleigh one. Second, the difference between the two tsunamis is not simply a matter of scaling the sub-Rayleigh rupture to generate a slip equal to the supershear one. If it was an issue of scaling, the ratio between the time histories in the two cases would have been the same throughout. Rather, it is evident that different features in the time histories from the two tsunamis have different relative amplitudes. For reference, the maximum slip in the simulated supershear rupture is 8.4 m, while the corresponding value in the sub-Rayleigh rupture is 6.3 m. However, the tsunami waves generated by the supershear rupture have amplitudes at peak values that range between one and four times as large as the one generated by the sub-Rayleigh one. This suggests that there exists a synergistic effect between the details of the dynamic rupture in both modes, the relative amplitude of fault parallel and fault normal components of displacements, the motion of the bathymetry, and the subsequent water level motion.

To emphasize the role of horizontal displacements on the induced tsunami, we compare the supershear earthquake-induced tsunami for three cases: (1) in a bay with all of the three components of the seafloor motion contributing to the bathymetry deformation, (2) in a bay with only the vertical component of the sea floor motion being considered, and, (3) in an open ocean with a flat bathymetry of constant depth.

Fig.6a illustrates the response at station S-1 in the three cases. For case (1), in which all components of motion are considered, we observe the arrival of the dynamic tsunami phase, then a co-seismic tsunami phase, followed by the classical postseismic tsunami wave, and then the radially propagating diffracted water front. On the contrary, the time history for case (2), in which only the vertical component of sea floor motion is included, indicates a weak tsunami signal. The dynamic tsunami signature, associated with the passage of the shock waves,is identical to that is observed for case (1). However, the subsequent classical tsunami is much smaller than in case (1). The classical tsunami in case (2) is generated by the waves set up at the fault with an amplitude determined by the residual displacements from the dynamic rupture as usually assumed

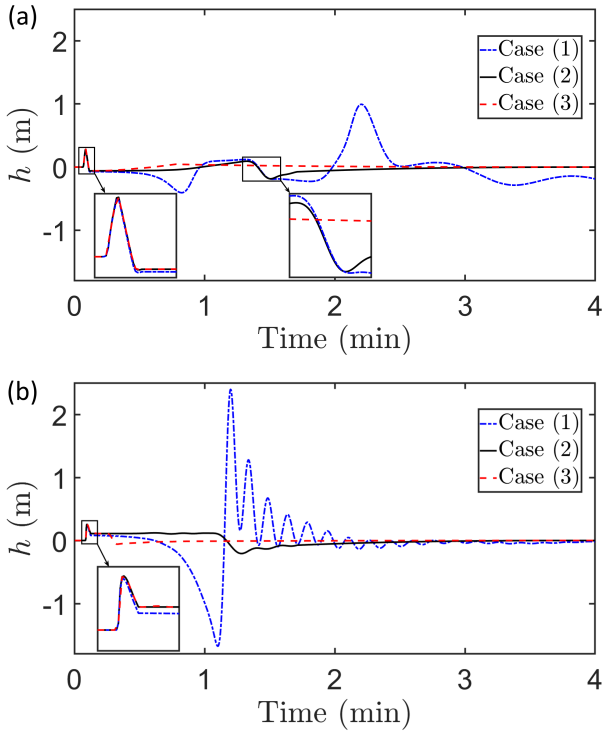

Fig. 6. The effect of including the horizontal motion on a basin bathymetry for a bay traversed by a super-shear rupture. The blue dash-dot line corresponds to the water level time history when all motions are included (Case 1). The solid black line shows the water level time history when horizontal motions are excluded (Case 2) The red-dashed line shows the water level time history in the open ocean with a flat bathymetry of constant depth (Case 3). The time histories are shown at stations (a) S-1, and (b) S-2.The dynamic tsunami phase at both stations are highlighted with zoom in. A segment of the classical tsunami phase at station S-1 around t 90 s is also highlighted in an insert

in the literature (28, 46, 52, 53). These waves have relatively small amplitude and upon propagation to the coastline, they are only weakly amplified as they run up the slope. For comparison, we also include the time history for the water surface amplitude in case (3) where the depth is uniform. In this case, we again see an identical signature of the dynamic tsunami corresponding to the passage of the shear shock wave fronts. This is then followed by the classical tsunami wave set up by the residual displacement field near the fault surface. Unlike cases 1 and 2, these waves are not amplified further since the water depth is uniform. The waves simply pass by the observation station and the recorded water level amplitude subsequently decays to zero.

In the absence of horizontal motion, Fig.6b further demonstrates that there is no substantial water uplift or depression. In the presence of horizontal displacements, the tsunami wave height may reach several meters and the water sea surface may change rapidly over a few seconds. These observations point to the critical role of horizontal motions in tsunami generation by strike slip faults. The large horizontal motions characteristic of supershear earthquakes (34, 37) on long strike slip faults may cause significant displacement to the coastline or bay bathymetry leading to vertical displacements of the water surface that may challenge those resulting from normal faulting. Strike slip faults traversing narrow bays or heading towards coastlines, may thus pose significant tsunami hazard even in the absence of landslides.

Conclusions

Our results suggest that strike slip faults, unlike what is typically assumed(16, 54, 55), may cause large tsunamis without the need to trigger underwater landslides. These results are based on numerical simulations of simple dynamic rupture scenarios on planar faults traversing a bay with idealized and smooth geometry. In that respect, our results are not masked by complex topography or complicated ground motions. Rather, they reveal some intrinsic mechanisms through which strike slip faults may become tsunamigenic.

Our model identifies several distinct features of tsunamis generated by strike slip faults traversing narrow bays. Notably, we recognize three distinct phases in the associated wave motions : (1) an instantaneous dynamic phase that is advected by the the elastodynamic field emanating from the dynamic rupture. The speed of propagation of this phase is several kilometers per seconds and hence it reaches the coastal areas synchronously with the shaking. (2)a co-seismic tsunami phase that emerges while the dynamic rupture is still active but propagates at a much slower speed than the dynamic tsunami phase due to the diminishing effect of sea floor velocities with time, and (3) a gravity driven post-seismic phase, which takes tens of seconds to several minutes to affect the coastal region. This phase, which carries memory of the histories of both the dynamic and coseismic tsunamis, is probably the most hazardous of the three phases due to its propensity to focusing effects at the apex,

diffraction by the bay geometry, and amplification by the bathymetry. The classification of tsunami motions we are introducing here may be potentially helpful in deciphering the multiple time scales observed in near source tsunami records.

Strike–slip faults usually generate large horizontal displacements but limited vertical displacements. It turns out that the positioning of the strike–slip fault with respect to the coastline is critical in leveraging these larger horizontal displacement in tsunami generation. Specifically, if the strike slip fault is located near the shore and is positioned such that it traverses a bay area or is heading towards the coastline, the tsunami hazard is amplified. The presence of an apex at the tip of a bay, further amplifies this effect since it results in wave focusing, and backward diffraction enabling multiple interactions with the slopes of the bay. The reason for this phenomenon is that in such geometries, the fault normal and fault parallel components of ground motion will cause horizontal deformations in the shoreline slopes that will in turn lead to vertical displacement of the water surface. If the slopes are steep enough, the resulting disturbance in the water surface may be significant. The effect of coupling between the horizontal motion and water level uplift has long been recognized for tsunamis induced by subduction zone earthquakes (56–58). The effect, however, has not been emphasized for strike–slip faults. We note that this effect may be non–negligible, and overlooking it in the case of strike slip faults may lead to a gross underestimation of their tsunami hazard.

Another important conclusion of our work is that the details of rupture propagation matter. Supershear ruptures are capable of generating larger tsunamis than sub-Rayleigh ruptures for the same rupture area. The shock wave fronts, which emerge during supershear propagation, carry in-plane and out-of-plane dynamic seafloor displacements and velocities to large distances away from the fault without significant attenuation(32, 36, 37). They also are more efficient in focusing energy ahead of the rupture tip and along the direction of propagation. These focused unattenuated displacements result in a stronger interaction between the dynamic earthquake motion and shoreline bathymetry, especially at the apex of bays, during the dynamic and coseismic phases of the tsunami. This in turn sets up higher water surface displacements which subsequently get further amplified as they run up the slopes. While for the same fault area, sub-Rayleigh ruptures produce smaller slip than supershear ruptures, the reduction in slip alone does not explain the smaller tsunami wave heights in the sub-Rayleigh case. Rather, our results suggest that the full history of the source dynamics, which also result in different spatial distributions of the final slip and ground motions, is critical to explain such discrepancy. This further motivates the need for integrated dynamic rupture-tsunami models like the one adapted here.

Since our modeling has used generic features of the earthquake and tsunami sources, we expect that our results are not per se location specific. Supershear rupture propagation, other similar bay geometries, and horizontal displacements of shoreline slopes, all may combine to produce tsunami amplification from strike–slip faults in different geographic areas. Potential candidates include the San Francisco Bay and the Tomales bay in Northern California, the Izmit bay in Turkey (which is crossed by the North Anatolian fault) and Al—Aqaba bay in Egypt (crossed by the Dead Sea Transform fault system). Just as in Palu Bay, tsunamis have been reported in these regions in the past, (23, 59–62) and have also had supershear rupture earthquake scenarios (20, 63, 64). We thus recommend revisiting the tsunami hazard rating of large submarine strike slip faults, particularly, those traversing narrow bays.

Materials and Methods

We used the crustal deformation finite element software Pylith for the earthquake rupture simulations. Pylith has been verified using community driven benchmarks, which are in line with SCEC/USGS Dynamic Rupture Code Verification exercises and can be obtained at (https://geodynamics.org/cig/software/pylith)(65). More details on the elastodynamic governing equations, as well as, simulation parameters are available in SI Appendix S1. The tsunami generation and propagation was conducted using SWIM, an in-house partial differential equation solver built on MOOSE framework(66). This nonlinear solver discretizes the shallow water equations spatially using finite element method and implicit time stepping for time integration. The tsunami is generated by the time-dependant motion of the bathymetry imported from the 3D dynamic rupture model in Pylith. A more detailed description of the tsunami model setup is given in SI Appendix S2. Furthermore, SWIM is verified using several benchmark problems in the literature (67–69). An example of the verification is presented in SI Appendix S3.

ACKNOWLEDGMENTS. A.E. acknowledges support by the National Science Foundation (CAREER Award Number 1753249). and A.J.R. acknowledges support by the Caltech/MCE Big Ideas Fund (BIF), as well as the Caltech Terrestrial Hazard Observation and Reporting Center (THOR). This research is part of the Blue Waters sustained–petascale computing project, which is supported by the National Science Foundation (awards OCI–0725070 and ACI–1238993) the State of Illinois, and as of December, 2019, the National Geospatial–Intelligence Agency. Blue Waters is a joint effort of the University of Illinois at Urbana-Champaign and its National Center for Supercomputing Applications. H. S. B. would like to acknowledge ERC Consolidator Grant PERSISMO a865411) for financial support. C.E.S thanks the National Science Foundation for Award Number 1906162, Field Survey of the 27 September 2018 Sulawesi Tsunami.

1. U Kânoğlu, V Titov, E Bernard, C Synolakis, Tsunamis: Bridging science, engineering and society. *Philos. Transactions Royal Soc. A: Math. Phys. Eng. Sci.* **373**, 20140369 (2015).
2. C Synolakis, E Okal, 1992–2002: Perspective on a Decade of Post-Tsunami Surveys in *Tsunamis*. (Springer-Verlag, Berlin/Heidelberg), pp. 1–29 (year?).
3. K Satake, EA Okal, JC Borrero, Tsunami and its Hazard in the Indian and Pacific Oceans: Introduction in *Tsunami and Its Hazards in the Indian and Pacific Oceans*. (Birkhäuser Basel, Basel) Vol. 110, pp. 249–259 (2017).
4. D McKenzie, J Jackson, Tsunami earthquake generation by the release of gravitational potential energy. *Earth Planet. Sci. Lett.* **345-348**, 1–8 (2012).
5. MR Legg, JC Borrero, CE Synolakis, Tsunami Hazards From Strike-Slip Earthquakes in *AGU Fall Meeting Abstracts*. Vol. 2003, pp. OS21D–06 (2003).
6. M Carvajal, C Araya-Cornejo, I Sepúlveda, D Melnick, JS Haase, Nearly Instantaneous Tsunamis Following the Mw 7.5 2018 Palu Earthquake. *Geophys. Res. Lett.* **46**, 5117–5126 (2019).
7. A Muhari, F Imamura, T Arikawa, AR Hakim, B Afriyanto, Solving the Puzzle of the September 2018 Palu, Indonesia, Tsunami Mystery: Clues from the Tsunami Waveform and the Initial Field Survey Data. *J. Disaster Res.* **13**, sc20181108 (2018).
8. Y Altinok, et al., The tsunami of August 17, 1999 in Izmit Bay, Turkey. *Nat. Hazards* **24**, 133–146 (2001).
9. AC Yalciner, et al., Tsunami Waves in Izmit Bay. *Earthq. Spectra* **16**, 55–62 (2000).
10. CE Synolakis, et al., The slump origin of the 1998 Papua New Guinea Tsunami. *Proc. Royal Soc. London. Ser. A: Math. Phys. Eng. Sci.* **458**, 763–789 (2002).
11. S Tinti, E Bortolucci, C Chiavettieri, Tsunami Excitation by Submarine Slides in Shallow-water Approximation. *Pure Appl. Geophys.* **158**, 759–797 (2001).

12. F Imamura, et al., Field survey of the 1994 Mindoro Island, Philippines tsunami. *Pure Appl. Geophys. PAGEOPH* **144**, 875–890 (1995).
13. S Sassa, T Takagawa, Liquefied gravity flow-induced tsunami: first evidence and comparison from the 2018 Indonesia Sulawesi earthquake and tsunami disasters. *Landslides* **16**, 195–200 (2019).
14. H Bao, et al., Early and persistent supershear rupture of the 2018 magnitude 7.5 Palu earthquake. *Nat. Geosci.* **12**, 200–205 (2019).
15. A Socquet, J Hollingsworth, E Pathier, M Bouchon, Evidence of supershear during the 2018 magnitude 7.5 Palu earthquake from space geodesy. *Nat. Geosci.* **12**, 192–199 (2019).
16. E Oral, H Weng, JP Ampuero, Does a Damaged-Fault Zone Mitigate the Near-Field Impact of Supershear Earthquakes?—Application to the 2018 Mw 7.5 Palu, Indonesia, Earthquake. *Geophys. Res. Lett.* **47**, 1–9 (2020).
17. K Nakata, A Katsumata, A Muhari, Submarine landslide source models consistent with multiple tsunami records of the 2018 Palu tsunami, Sulawesi, Indonesia. *Earth, Planets Space* **72**, 44 (2020).
18. AL Williamson, D Melgar, X Xu, C Milliner, The 2018 Palu Tsunami: Coeval Landslide and Coseismic Sources. *Seismol. Res. Lett.* **91**, 3148–3160 (2020).
19. T Ulrich, et al., Coupled, Physics-Based Modeling Reveals Earthquake Displacements are Critical to the 2018 Palu, Sulawesi Tsunami. *Pure Appl. Geophys.* **176**, 4069–4109 (2019).
20. F Amlani, et al., Supershear Tsunamis: Insights from the $ M_ ${$w$}$ $7.5 Palu Earthquake. *arXiv preprint arXiv:1910.14547* (2019).
21. VV Titov, CE Synolakis, Numerical Modeling of Tidal Wave Runup. *J. Waterw. Port, Coastal, Ocean. Eng.* **124**, 157–171 (1998).
22. TM Niemi, NT Hall, Historical changes in the tidal marsh of Tomales Bay and Olema Creek, Marin County, California. *J. Coast. Res.* **12**, 90–102 (1996).
23. N Lyberis, Tectonic evolution of the Gulf of Suez and the Gulf of Aqaba. *Tectonophysics* **153**, 209–220 (1988).
24. S Özalaybey, et al., The 1999 İzmit earthquake sequence in Turkey: Seismological and tectonic aspects. *Bull. Seismol. Soc. Am.* **92**, 376–386 (2002).
25. J Lauterjung, U Münch, A Rudloff, The challenge of installing a tsunami early warning system in the vicinity of the Sunda Arc, Indonesia. *Nat. Hazards Earth Syst. Sci.* **10**, 641–646 (2010).
26. PL Liu, X Wang, AJ Salisbury, Tsunami hazard and early warning system in South China Sea. *J. Asian Earth Sci.* **36**, 2–12 (2009).
27. L Mansinha, DE Smylie, The Displacement Fields of Inclined Faults. *Bull. - Seismol. Soc. Am.* **61**, 1433–1440 (1971).
28. Y Okada, Internal deformation due to shear and tensile faults in a half-space. *Bull. - Seismol. Soc. Am.* **82**, 1018–1040 (1992).
29. Y Kervella, D Dutykh, F Dias, Comparison between three-dimensional linear and nonlinear tsunami generation models. *Theor. Comput. Fluid Dyn.* **21**, 245–269 (2007).
30. GC Lotto, EM Dunham, High-order finite difference modeling of tsunami generation in a compressible ocean from offshore earthquakes. *Comput. Geosci.* **19**, 327–340 (2015).
31. KJ Ryan, EL Geist, M Barall, DD Oglesby, Dynamic models of an earthquake and tsunami offshore Ventura, California. *Geophys. Res. Lett.* **42**, 6599–6606 (2015).
32. AJ Rosakis, O Samudrala, D Coker, Cracks Faster than the Shear Wave Speed. *Science* **284**, 1337–1340 (1999).
33. AJ Rosakis, Intersonic shear cracks and fault ruptures. *Adv. Phys.* **51**, 1189–1257 (2002).
34. EM Dunham, RJ Archuleta, Evidence for a supershear transient during the 2002 Denali fault earthquake. *Bull. Seismol. Soc. Am.* **94**, 256–268 (2004).
35. EM Dunham, Conditions governing the occurrence of supershear ruptures under slip-weakening friction. *J. Geophys. Res.* **112**, B07302 (2007).
36. EM Dunham, HS Bhat, Attenuation of radiated ground motion and stresses from three-dimensional supershear ruptures. *J. Geophys. Res. Solid Earth* **113**, 1–17 (2008).
37. M Mello, HS Bhat, AJ Rosakis, H Kanamori, Reproducing the supershear portion of the 2002 Denali earthquake rupture in laboratory. *Earth Planet. Sci. Lett.* **387**, 89–96 (2014).
38. X Ma, A Elbanna, Effect of off-fault low-velocity elastic inclusions on supershear rupture dynamics. *Geophys. J. Int.* **203**, 664–677 (2015).
39. LB Freund, The mechanics of dynamic shear crack propagation. *J. Geophys. Res. Solid Earth* **84**, 2199–2209 (1979).
40. DJ Andrews, Rupture Velocity of Plane Strain Shear Cracks. *J Geophys. Res* **81**, 5679–5687 (1976).
41. RJ Archuleta, Faulting Model for the 1979 Imperial Valley Earthquake. *J. Geophys. Res.* **89**, 4559–4585 (1984).
42. M Mello, HS Bhat, AJ Rosakis, Spatiotemporal properties of Sub-Rayleigh and supershear rupture velocity fields: Theory and experiments. *J. Mech. Phys. Solids* **93**, 153–181 (2016).
43. AJ Rosakis, V Rubino, N Lapusta, Recent Milestones in Unraveling the Full-Field Structure of Dynamic Shear Cracks and Fault Ruptures in Real-Time: From Photoelasticity to Ultrahigh-Speed Digital Image Correlation. *J. Appl. Mech.* **87**, 1–17 (2020).
44. U Kânoğlu, C Synolakis, Initial Value Problem Solution of Nonlinear Shallow Water-Wave Equations. *Phys. Rev. Lett.* **97**, 148501 (2006).
45. VV Titov, CE Synolakis, Extreme inundation flows during the Hokkaido-Nansei-Oki Tsunami. *Geophys. Res. Lett.* **24**, 1315–1318 (1997).
46. Y Tanioka, K Satake, Tsunami generation by horizontal displacement of ocean bottom. *Geophys. Res. Lett.* **23**, 861–864 (1996).
47. D Dutykh, D Mitsotakis, LB Chubarov, YI Shokin, On the contribution of the horizontal sea-bed displacements into the tsunami generation process. *Ocean. Model.* **56**, 43–56 (2012).
48. A Hooper, et al., Importance of horizontal seafloor motion on tsunami height for the 2011 Mw=9.0 Tohoku-Oki earthquake. *Earth Planet. Sci. Lett.* **361**, 469–479 (2013).
49. EL Geist, T Parsons, Triggering of tsunamigenic aftershocks from large strike-slip earthquakes: Analysis of the November 2000 New Ireland earthquake sequence. *Geochem. Geophys. Geosystems* **6**, n/a–n/a (2005).
50. V Rubino, AJ Rosakis, N Lapusta, Spatiotemporal Properties of Sub-Rayleigh and Supershear Ruptures Inferred From Full-Field Dynamic Imaging of Laboratory Experiments. *J. Geophys. Res. Solid Earth* **125**, 1–25 (2020).
51. G Masselink, P Russell, Flow velocities, sediment transport and morphological change in the swash zone of two contrasting beaches. *Mar. Geol.* **227**, 227–240 (2006).
52. EA Okal, CE Synolakis, A theoretical comparison of tsunamis from dislocations and landslides. *Pure Appl. Geophys.* **160**, 2177–2188 (2003).
53. EL Geist, DD Oglesby, Earthquake Mechanism and Seafloor Deformation for Tsunami Generation in *Encyclopedia of Earthquake Engineering*, eds. M Beer, IA Kougioumtzoglou, E Patelli, ISK Au. (Springer Berlin Heidelberg, Berlin, Heidelberg), pp. 1–17 (2014).
54. JC Borrero, MR Legg, CE Synolakis, Tsunami sources in the southern California bight. *Geophys. Res. Lett.* **31**, n/a–n/a (2004).
55. CE Synolakis, AC Yalciner, JC Borrero, G Plafker, Modeling of the November 3, 1994 Skagway, Alaska Tsunami in *Solutions to Coastal Disasters '02*. (American Society of Civil Engineers, Reston, VA), Vol. 40605, pp. 915–927 (2002).
56. J Polet, H Kanamori, Shallow subduction zone earthquakes and their tsunamigenic potential. *Geophys. J. Int.* **142**, 684–702 (2000).
57. M Heidarzadeh, A Kijko, A probabilistic tsunami hazard assessment for the Makran subduction zone at the northwestern Indian Ocean. *Nat. Hazards* **56**, 577–593 (2011).
58. T Baba, PR Cummins, T Hori, Y Kaneda, High precision slip distribution of the 1944 Tonankai earthquake inferred from tsunami waveforms: Possible slip on a splay fault. *Tectonophysics* **426**, 119–134 (2006).
59. A Pinar, N Türkelli, Source inversion of the 1993 and 1995 Gulf of Aqaba earthquakes. *Tectonophysics* **283**, 279–288 (1997).
60. PM Mai, Supershear tsunami disaster. *Nat. Geosci.* **12**, 150–151 (2019).
61. M Barjous, S Mikbel, Tectonic evolution of the gulf of Aqaba-Dead Sea transform fault system. *Tectonophysics* **180**, 49–59 (1990).
62. E Frucht, et al., A fresh view of the tsunami generated by the dead sea transform, 1995 Mw 7.2 Nuweiba earthquake, along the Gulf of Elat–Aqaba. *Seismol. Res. Lett.* **90**, 1483–1493 (2019).
63. M Bouchon, et al., How fast is rupture during an earthquake? New insights from the 1999 Turkey Earthquakes. *Geophys. Res. Lett.* **28**, 2723–2726 (2001).
64. SG Song, GC Beroza, P Segall, A Unified Source Model for the 1906 San Francisco Earthquake. *Bull. Seismol. Soc. Am.* **98**, 823–831 (2008).
65. B Aagaard, C Williams, M Knepley, geodynamics/pylith: PyLith v2.2.1. (2017).
66. CJ Permann, et al., {MOOSE}: Enabling massively parallel multiphysics simulation. *SoftwareX* **11**, 100430 (2020).
67. M Derakhti, RA Dalrymple, EA Okal, CE Synolakis, Temporal and Topographic Source Effects on Tsunami Generation. *J. Geophys. Res. Ocean.* **124**, 5270–5288 (2019).
68. JL Hammack, A note on tsunamis: Their generation and propagation in an ocean of uniform depth. *J. Fluid Mech.* **60**, 769–799 (1973).
69. TS Stefanakis, F Dias, C Synolakis, Tsunami Generation Above a Sill. *Pure Appl. Geophys.* **172**, 985–1002 (2015).
70. R Dalrymple, B Rogers, Numerical modeling of water waves with the SPH method. *Coast. Eng.* **53**, 141–147 (2006).

Appendix

Earthquake Model Setup. The earthquake is initiated in a 3-D domain of dimensions $(x_1, x_2, x_3) \in (0, 60) \times (-15, 15) \times (-0.7, -15)$ km with a planar fault located at $x_2 = 0$. The mesh we used included 216 million elements to spatially discretize the domain with an element size of $50 \times 50 \times 50$ m. The choice of the element size was made such that the fundamental elasto-frictional length scale was properly resolved by 8 elements. Temporally, we used explicit forward Euler time integration with time step controlled by the CFL condition.

The linear elastodynamics is described by a system of time-dependent field equations subject to suitable initial and boundary conditions related to a body transmitting elastic waves. The governing equations are given by:

$$\sigma_{ij,j} + b_i = \rho \ddot{u}_i \tag{3}$$

Where, σ_{ij} correspond to the stress state, b_i are the body forces, and $\ddot{u}_i$ is the second time derivative of the displacement field. For a linear isotropic material the constitutive relation becomes:

$$\sigma_{ij} = \lambda \delta_{ij} \varepsilon_{kk} + 2\mu \varepsilon_{ij} \tag{4}$$

where ε_{ij} is the strain tensor, and μ, and λ are the Lamé parameters, the model constitutive parameters are given in Table 1. In the limit of small deformation the strain can be expressed in terms of the displacement field u_i as:

$$\varepsilon_{ij} = \frac{1}{2}\left[u_{i,j} + u_{j,i}\right] \tag{5}$$

The fault slippage is governed a slip-weakening friction model. The shear tractions T_f is described in terms of cohesive traction T_c, slip d, and fault normal traction T_n as:

$$T_f = \begin{cases} T_c - \left[\mu_s - (\mu_s - \mu_d)\frac{d}{d_o}\right] T_n & \text{for } d \le d_o \text{ and } T_n \le 0 \\ T_c - \mu_d T_n & \text{for } d > d_o \text{ and } T_n \le 0 \end{cases} \tag{6}$$

Here, μ_s is the static coefficient of friction, μ_d is the dynamic coefficient of friction, and characteristic slip weakening distance d_o. The frictional properties are distributed along the depth, such that there is locked-slipping interface located below $x_3 = -11$ km.

For supershear rupture case, Above 11 km, the fault frictional parameters are $\mu_s = 0.6$, $\mu_d = 0.3$ for the static and dynamic friction coefficients, respectively, and $d_o = 0.2$ for the slip weakening distance. The stress is initially distributed over the fault surface as $T_n = -50$ MPa , and $T_f = 24$ MPa. However, the shear stress is locally increased within the overstressed region and $T_f = 31$ MPa. The fault stresses and properties outside the overstressed region correspond to a strength parameter $S = 0.667$.

For the sub–Rayleigh rupture case, above 11 km, the fault frictional parameters are identical to those in the supershear case. However, the fault shear stress is initially distributed to a value $T_f = 31$ within the overstressed patch, and a value of $T_f = 19.2$ outside the overstressed region, respectively. The normal compressive stresses are uniform throughout and taken to be $T_n = -50$ MPa, identical to the supershear case. In this case, the fault stresses and properties outside the overstressed region correspond to a strength parameter $S = 2.62$. The higher value of the S parameter generally favors sub-Rayleigh rupture propagation and significantly delays the supershear transition, if it is to occur.

Tsunami Model Setup. For the tsunami modelling, we consider the nonlinear shallow water wave approximation for incompressible flow with constant density ρ in a domain $\Omega \in \mathbf{R}^2$ governed by Eq.1 for $\forall t \in [0, T]$. A Cartesian coordinate system is chosen such that the $x_3 = 0$ correspond undisturbed water level, and $x_1, x_2 = 0$ correspond to the hypocenter of the dynamic rupture. For the tsunami model the domain of the problem is defined by $(x_1, x_2) \in (0, L) \times (-W/2, W/2)$, the discretization of tsunami domain is independent of the solid domain, a uniform mesh with element size 25 m was used for spatial discretization. Temporally, the solutions of the shallow water equations evolve at a different time scale than dynamic rupture. We thus allow, within our unconditionally stable MOOSE-SWIM implicit Euler solver, for a different time step in the tsunami model, constrained by the accuracy requirements. We have also run the simulations at different time resolutions to check for convergence.

The following boundary conditions were imposed on shallow water equation 1:

$$\hat{u}(x_1 = L, x_2, t) = 0 \tag{7a}$$

$$\hat{v}(x_1, x_2 = W/2, t) = \hat{v}(x_1, x_2 = -W/2, t) = 0 \tag{7b}$$

$$h_{,2}|_{W/2} = h_{,2}|_{-W/2} = 0 \tag{7c}$$

$$h_{,1}|_{L} = 0 \tag{7d}$$

The basin-like static bathymetry utilized in our tsunami model as demonstrated in Fig.2a is defined as $H_o(x_i) = a + (b - a)F_o(x_i)$, where F_o is a hyperbolic tangent function given by the following equation:

$$F_o(x_i) = \begin{cases} \frac{1}{2}(1 - \tanh\frac{r - r_c}{s}), & \text{for } x_1 \ge c \\ \frac{1}{2}(1 - \tanh\frac{|x_2| - r_c}{s}), & \text{for } x_1 \le c \end{cases} \tag{8}$$

Here, a, b are the minimum and maximum depth respectively, r_c is the radius of the basin, c is the center point of the bay apex and s is a constant that defines the slope of the bay. We choose this generic bathymetry to decouple our conclusions from any effect of shoreline geometric complexity that may mask tsunami dynamics.

The choice of the 2-D domain and bathymetry for the tsunami model has been motivated by the Palu bay. The simulated domain has the following dimensions $L = 37$ km and $W = 5$ km, and bathymetry parameters of minimum depth $a = 10$ m and maximum depth $b = 700$ m. We chose the following parameters for the basin, the radius is $r_c = 3$ km, and slope constant $s = 400$, with center $c = 30.5$ km. This specific choice of the s results in a slope varying from 700 m to 10 m over to a 2 km distance.

SWIM Verification. To validate our SWIM implementation, we solve the nonlinear shallow water equation against the "piston" motion described in Derakhti et al. (2019) (67). Derakhti et al. (2019) used the Smooth Particle Hydrodynamics (SPH) method of Dalrymple and Rogers (2006) (70), and validated their results using experimental data from Hammack (1973). For reference, our SWIM code solves the NSWE in an incompressible inviscid domain assuming depth–averaged variables. The validation against the SPH method and the laboratory results allows for checking the veractiry of SWIM and the adequacy of the NSWE approximation, particularly when gauging the influence of a dynamically moving sea bed.

We solve the 1D nonlinear shallow water equation with identical geometry to the domain setup in the x-z plane as in Derakhti et al. (2019). The seafloor displacement $U_3(t)$ is the following:

$$u_3(x_1,t) = \begin{cases} 0 & \text{for } t < 0 \\ \frac{1}{2}u_m\left[1-\cos\frac{\pi t}{t_r}\right]\mathcal{H}(b_o^2 - x_1^2) & \text{for } 0 \le t \le t_r \\ u_m\mathcal{H}(b_o^2 - x_1^2) & \text{for } t > t_r \end{cases} \quad [9]$$

Here, the ocean depth is H and a portion of the seafloor with half–width b_o is displaced upward for a total distance u_m, over the rise time t_r. The width of the seafloor displacement is imposed through $\mathcal{H}$ the Heaviside step function. Following Derakhti et al. (2019), a number of dimensionless quantities are introduced to define the loading rate, namely, $t_c = b_o/\sqrt{gH}$, and $\tau = t_r/t_c$, note that for a similar setup a lower τ indicate a faster rise time t_r.

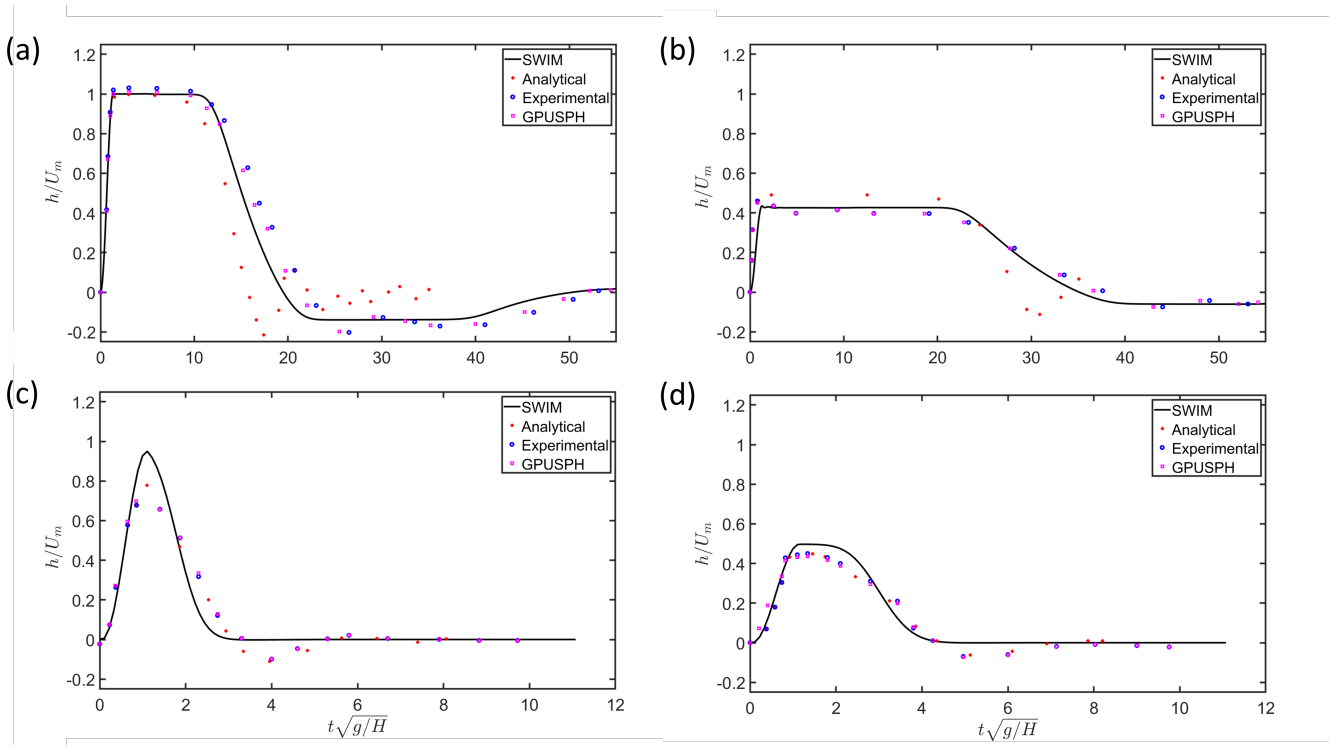

Fig. S 1. Benchmark problem verification of the shallow water wave implementation (SWIM code) used in the present study, compared with the predictions of experiments and analytical, and numerical solutions from the literature (67, 68) .The comparison shows the normalized time history of water surface level, h, for a punch, initially at rest at the sea floor and subsequently driven upward with hyperbolic cosine velocity profile. (a-b) Impulsive and (c-d) milder (transitional) bed displacements. The undisturbed water depth is H.

To explore the impact of the loading rate, we compare two cases with the numerical solution from Derakhti et al. (2019) and the experimental results from Hammack (1973): (1) Impulsive loading with $\tau = 0.11$, and $u_m/H = 0.4$, (2) Transitional loading with $\tau = 0.9$, and $u_m/H = 0.01$. Fig.1a illustrate the different normalized sea surface displacement h/u_m at $x_1/b_o = 0$ corresponding to the center of the seafloor. The shallow water equation compares well in terms of maximum amplitude as well as the trailing wave behavior. Fig.1b demonstrate better agreement for the near the far edge of seafloor displacement at $x_1/b_o = 1$. For case (2) with transitional loading, we observe in Fig.1c deviations in the peak amplitude at the center of the seafloor displacement. This discrepancy is attributed to the low u_m/H parameter, indicating further deviation from the shallow water limit. Similarly, the results further away from the center of the seafloor displacement show better agreement, as illustrated in Fig.1d.

Furthermore, lack of oscillations is observed in the shallow water solution when compared with SPH and experimental observations. This is attributed to the shallow water approximation. Such absence was also reported in Stefanakis et al. (69), who provided analytic solutions for the rise of a sill off the seafloor. Overall, the major features of the solution are still preserved, such as the rise time, peak amplitude and approach to steady state.

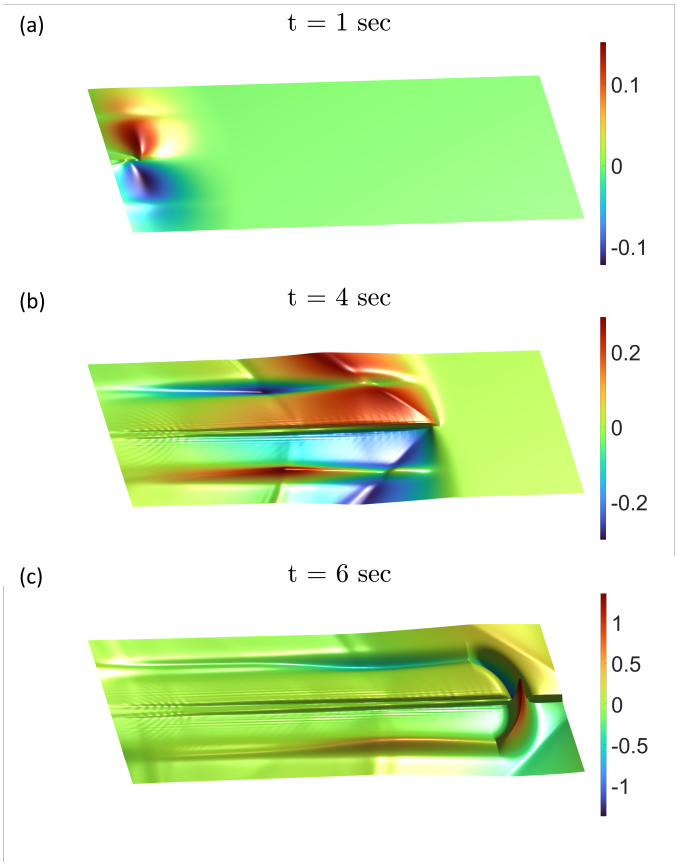

Fig. S 2. Benchmark problem verification of the shallow water wave implementation (SWIM code) used in the present study, compared with the predictions of experiments and analytical, and numerical solutions from the literature (67, 68) .The comparison shows the normalized time history of water surface level, h, for a punch, initially at rest at the sea floor and subsequently driven upward with hyperbolic cosine velocity profile. (a-b) Impulsive and (c-d) milder (transitional) bed displacements. The undisturbed water depth is H.

Table 1. Constitutive parameters for earthquake model

Medium Parameters	Values
1. Shear Modulus	32 GPa
2. S-wave speed, c_s	3.464 km s$^-1$
3. P-wave speed, c_p	6 km s$^-1$
3. Mass density, ρ	2670 kg m$^-3$

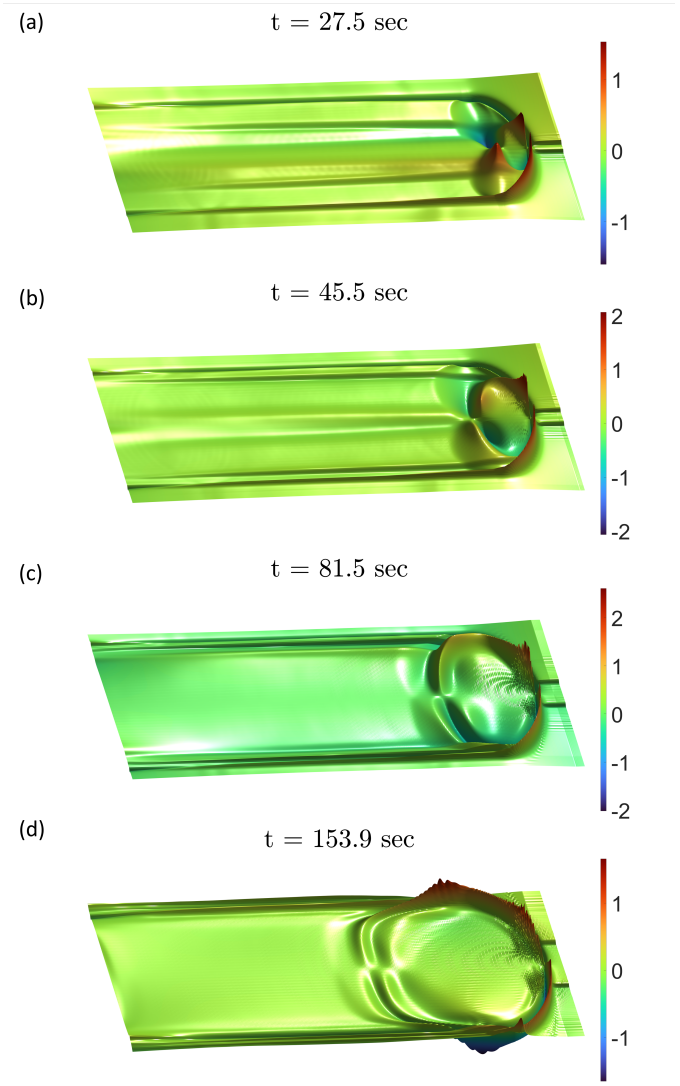

Fig. S 3. Benchmark problem verification of the shallow water wave implementation (SWIM code) used in the present study, compared with the predictions of experiments and analytical, and numerical solutions from the literature (67, 68) .The comparison shows the normalized time history of water surface level, h, for a punch, initially at rest at the sea floor and subsequently driven upward with hyperbolic cosine velocity profile. (a-b) Impulsive and (c-d) milder (transitional) bed displacements. The undisturbed water depth is H.

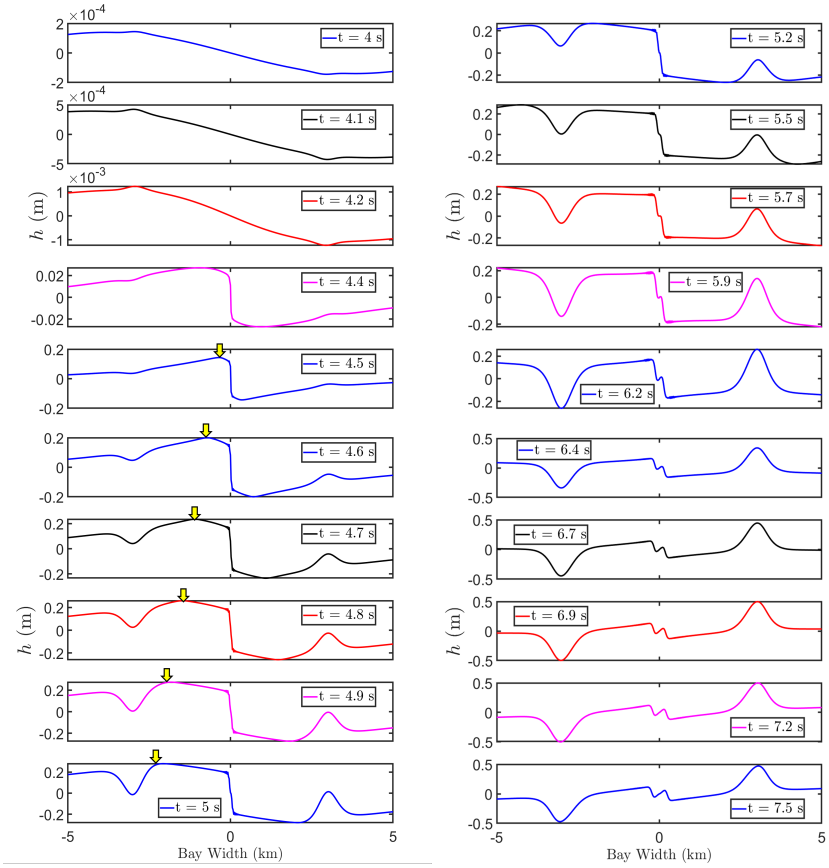

Fig. S 4. Snapshots of sea surface height h for cross section A-A during the dynamic tsunami phase. The snapshots capture in more details the evolution of the dynamic tsunami generation phase between times t = 4 s, and t = 7.5 s. The height scale varies according to the sea surface peak height at each displayed time. Between times t = 4.0 s and t= 4.4 s, the sea surface is perturbed by the dilatational wave field which propagates ahead of the rupture front and precedes the arrival of the shear shock wave fronts. The lack of any vertical displacement at x = 0 in the subplots for times t = 4.0 s, 4.1 s, and 4.2 s, is consistent with the fault surface being a nodal plane for the P-wave. Later, starting with time t = 4.4 s, we observe the development of a vertical offset at the location of the fault plane. This offset is the result of the vertical displacement carried by the rupture front which arrives at section A-A around t = 4.4 s. The vertical offset continues to develop in subsequent times (t = 4.4 s to t = 4.6 s) as the rupture tip propagates and the intense shear shock waves (Mach cones) cross section A-A at the location of the fault surface. This offset later disintegrates (time t = 5.2 s and later) into a pair of waves propagating in opposite directions towards the sides of the bay. As the rupture tip moves past section A-A, the Mach cone fronts intersect with section A-A at different points as they expand away from the fault plane (x = 0), and we highlight the effect of the Mach fronts on the sea surface height by the yellow arrows between times t = 4.5 s and t = 5.0 s. A local trough (crest) develops in the sea surface profile over the left (right) sides of the bay. These start with an initially small amplitude (t = 4.4 s) and continue to grow slowly afterwards (up to t = 5.0 s) until the Mach cone fronts intersect with section A-A at the location of the slopes leading to a rapid increase in the amplitude of these features. The trough and the crest develop due to the effect of the horizontal displacements that are induced by the dynamic sea floor motion which cause bathymetry deformation and subsequent vertical variation in the sea surface height as discussed in the main text. Initially (up to t = 5.0 s), the slopes of the bay experience small horizontal displacements. The source of these displacements are the dilatational wave field existing ahead of the rupture tip and the Mach fronts, as well as any shear or Rayleigh wavefields that have been generated during the early stages of the rupture nucleation and propagation before its transitioning into supershear. However, at later times (t > 5.0 s), the Mach cones arrive. The Mach cone fronts carry larger horizontal displacements leading to a rapid increase in the amplitude of the trough and crest (up to t = 6.9 s). Subsequently, as the Mach cones move away from sec A-A, the dynamic horizontal displacements decrease, and we observe a gradual reduction in the amplitude of the sea surface perturbations over the slope (t = 7.2 s and t = 7.5 s). The subsequent evolution the different tsunami features at later times is detailed in the main text as part of the discussion that follows Figure 3.